

Rising of the lowest place on Earth due to Dead Sea water-level drop: Evidence from SAR interferometry and GPS

R. N. Nof,^{1,2} A. Ziv,³ M.-P. Doin,⁴ G. Baer,² Y. Fialko,⁵ S. Wdowinski,⁶ Y. Eyal,¹ and Y. Bock⁵

Received 22 October 2011; revised 29 March 2012; accepted 15 April 2012; published 25 May 2012.

[1] The Dead Sea water-level has been dropping at an exceedingly increasing rate since 1960, and between 1993 and 2001, the interval of the InSAR data examined in this study, it has dropped at an average rate of 0.88 m per year. Such a water-level change could potentially give rise to a resolvable lithospheric rebound and regional uplift, with spatial extent and amplitude that are controlled by the effective mechanical properties of the crust and upper mantle combined. We measure that deformation for the years 1993 to 2001, using 149 short baseline interferograms made of 31 ERS-1 and ERS-2 Synthetic Aperture Radar (SAR) images and continuous GPS data from the Survey of Israel recorded between 1997 and 2011. The uplift rate at the Dead Sea is small (up to 4 mm/year), and the basin topography is almost a mirror of the displacement, introducing a strong trade-off between uplift and stratified atmosphere noise. To overcome this complication, we impose a linearity constraint on the satellite to ground Line Of Sight (LOS) phase changes based on the steady uplift observed by a continuous GPS station in the area of interest, and simultaneously solve for the LOS change rate, Digital Elevation Model (DEM) errors and the elevation-phase correlation. While the LOS rate and DEM errors are solved for each pixel independently, the elevation-phase correlation is solved for each SAR acquisition independently. Using this approach we separated the stratified atmospheric delay from the ground displacement. We observed a regional uplift around the Dead Sea northern basin, with maximum uplift close to the shorelines, and diminishing to zero by the Mediterranean coast. We modeled the effect of water load changes using a homogeneous elastic half-space, and found a good agreement between modeled and observed ground displacements using elastic properties that are compatible with seismic and gravity data down to a depth of 15 km below the Dead Sea basin, suggesting that the response of the crust to the sea level drop is controlled mainly by the elastic properties of the upper-crust immediately below the Dead Sea basin.

Citation: Nof, R. N., A. Ziv, M.-P. Doin, G. Baer, Y. Fialko, S. Wdowinski, Y. Eyal, and Y. Bock (2012), Rising of the lowest place on Earth due to Dead Sea water-level drop: Evidence from SAR interferometry and GPS, *J. Geophys. Res.*, 117, B05412, doi:10.1029/2011JB008961.

¹Department of Geological and Environmental Sciences, Ben-Gurion University of the Negev, Beer Sheva, Israel.

²Geological Survey of Israel, Jerusalem, Israel.

³Geophysics and Planetary Sciences, Raymond and Beverly Sackler Faculty of Exact Sciences, Tel-Aviv University, Tel-Aviv, Israel.

⁴Laboratoire de Géologie, École Normale Supérieure, CNRS, Paris, France.

⁵Scripps Institution of Oceanography, University of California, San Diego, La Jolla, California, USA.

⁶Division of Marine Geology and Geophysics, Rosenstiel School of Marine and Atmospheric Science, University of Miami, Miami, Florida, USA.

Corresponding author: R. N. Nof, Department of Geological and Environmental Sciences, Ben-Gurion University of the Negev, PO Box 653, Beer Sheva 84105, Israel. (ran.nof@gmail.com)

Copyright 2012 by the American Geophysical Union.
0148-0227/12/2011JB008961

1. Introduction

[2] Ground displacements caused by changes in surface load may be used to probe the crust and upper mantle rheology [e.g., *Peltier et al.*, 1986; *Bills and May*, 1987; *Lambeck*, 1991; *Mitrovica and Peltier*, 1993; *Lambeck et al.*, 1998; *Sjöberg et al.*, 2000]. Recent advances in space geodesy and processing techniques make it now possible to map a few kilometers long displacement patterns, with amplitudes of the order of a few centimeters. Here we map and discuss the geodynamic implications of the ground displacements associated with the water-level drop in the Dead Sea northern basin.

[3] The Dead Sea is located along the Dead Sea Transform (Figure 1), within a 250 km long topographic and structural depression that is filled by ~10 km thick Neogene to Quaternary sedimentary sequence. The Dead Sea is divided into two sub-basins: a northern basin that is 45 km long and 16 km

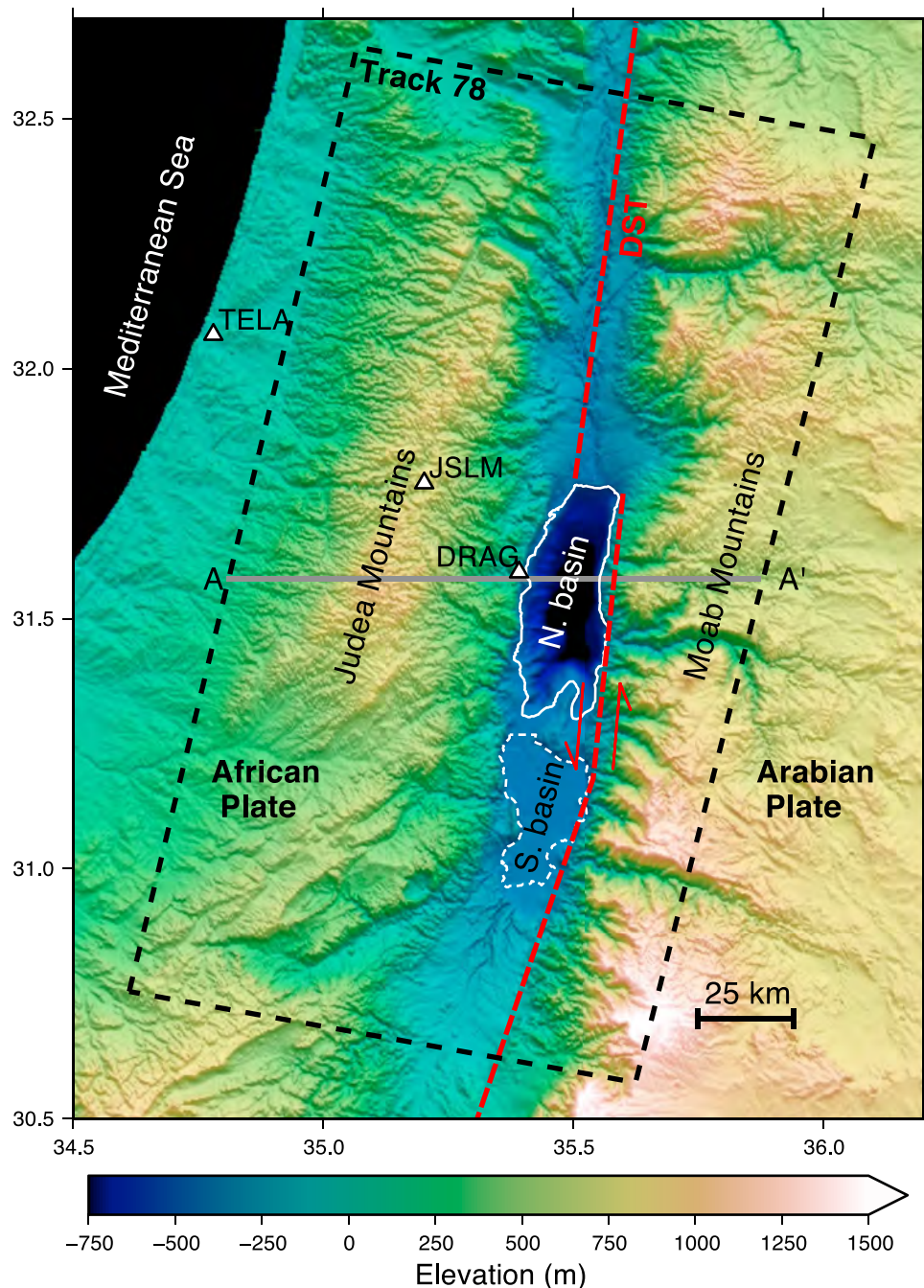


Figure 1. Location map. Track 78 (dashed black rectangle) is shown on a hill shaded DEM, composed of SRTM DEM and Dead Sea bathymetry of Hall [1996]. The Dead Sea northern basin is outlined by a white solid contour of 407 m below MSL (corresponds to the year 1993) and the southern basin is outlined by a white dashed contour of 380 m below MSL. The dashed red line marks the approximate location of the Dead Sea Transform (DST) trace. The white triangles mark the location of the three permanent GPS sites, whose velocities are shown in Figure 13. Profile A-A' (gray line) is shown in Figure 6.

wide, whose seafloor is at a depth of 700–730 m below Mean Sea Level (MSL), and a smaller and shallower southern basin occupied by artificial evaporation pans of the mineral industry [Hall, 1996]. Current sedimentation rate (mostly halite) within the northern basin is about 0.1 m per year [Lensky *et al.*, 2005]. Between 1980 and 2010 the water-level within the northern basin has dropped from -401.1 m to -422.3 m and between 1993 and 2001, the interval of the

InSAR data examined in this study, it dropped at an average rate of 0.88 m per year ([Hect and Gertman, 2003] Israel Hydrological Service database) (Figure 2). Such a water-level change may give rise to a resolvable lithospheric rebound, with magnitude and spatial extent that are controlled by the effective mechanical properties of the Earth's crust and upper mantle, as is observed in other areas of significant hydrologic loading [e.g., Nakiboglu and Lambeck,

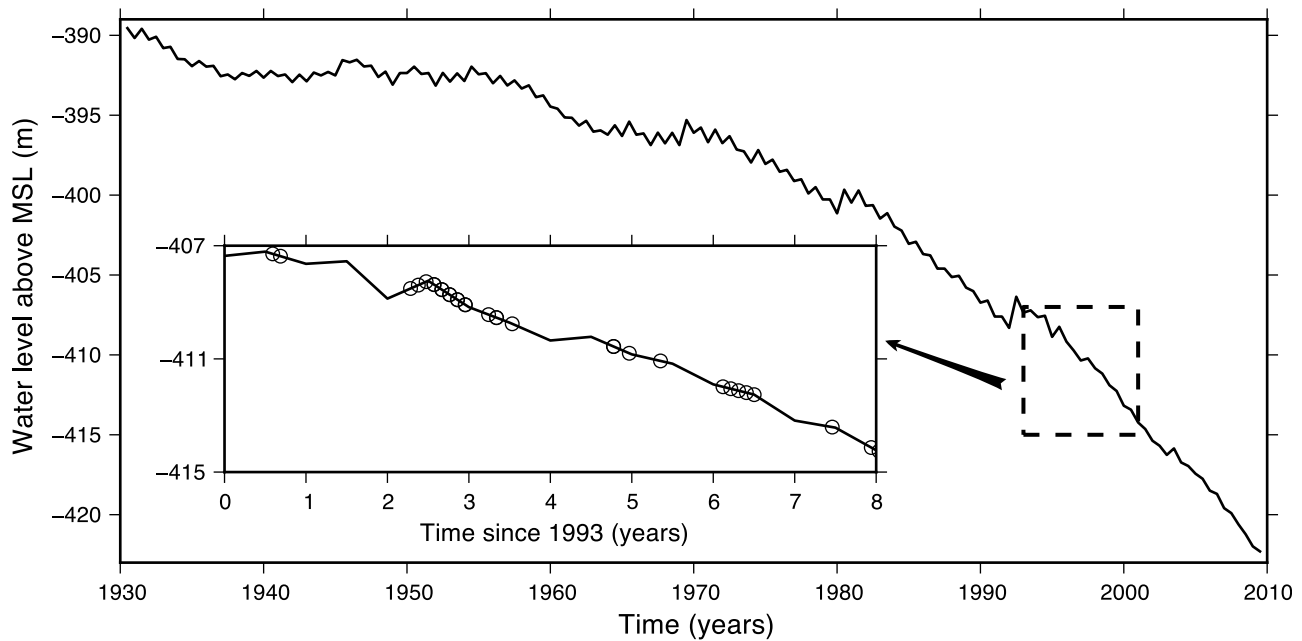


Figure 2. Dead Sea water-level changes relative to MSL (from Israel Hydrological Service database). Inset provides enlarged view of the interval analyzed in this study, with circles indicating satellite acquisition times.

1982]. For example, *Cavalié et al.* [2007] performed an Interferometric Synthetic Aperture Radar (InSAR) time series analysis of the Lake Mead area, and inferred a maximum subsidence of 16 mm due to 11 m of water-level rise. Using a similar approach, a bowl shape deformation pattern centered on Lake Siling Co in Tibet, extending to about 100 km from the lake center, with a maximum rate of 5 mm per year was identified by *Doin et al.* [2010].

[4] Several processes may contribute to the observed ground displacements. Understanding the different contributions to surface deformation and their spatiotemporal distribution is important for the identification of the ground displacement due to the sea level drop. The Dead Sea basin lies within an active left lateral transform [*Freund et al.*, 1970; *Garfunkel*, 1997], whose current slip rate and locking depth are about 5 mm per year and 15–20 km, respectively [*Wdowski et al.*, 2004; *Le Beon et al.*, 2008; *Sadeh*, 2011]. The contribution to the satellite line-of-sight (LOS) measurements of such slip rate along the Dead Sea transform cannot exceed 0.2 mm per year. Another deformation process is related to the replacement of saline water by non-saline groundwater, resulting in the dissolution of the salt layer at a depth between 20 and 50 m [*Wachs et al.*, 2000; *Baer et al.*, 2002; *Abelson et al.*, 2003]. This, in turn, causes occasional collapse of sink-holes up to a couple of kilometers from the Dead-Sea shoreline. An additional effect of water-level drop is pore compaction within the coastal mud flats. Thus, the interaction with groundwater is of very limited extent, and results in local subsidence. Finally, the rise of the salt diapirs within the study area is characterized by spatial extent that is much shorter than that related to the sea level drop. Some of the above deformation phenomena have already been quantified and mapped using InSAR measurements (sink-hole collapses: [*Baer et al.*, 2002;

Abelson et al., 2003]; diapir rise: [*Pe'eri et al.*, 2004; *Weinberger et al.*, 2006]).

[5] In this paper we investigate the deformation associated with the retreat of the Dead Sea level, using InSAR and continuous GPS measurements. We first describe the data selection criteria and the interferogram and GPS processing. We then present schemes for removing the phase contribution due to orbital errors and stratified atmosphere in the InSAR analysis. Next, we present a map of the deformation associated with the Dead Sea water-level drop, and finally we discuss the geodynamic and mechanic implications of the results.

2. Data Selection and Processing

2.1. InSAR

[6] We used all available SAR data from the descending track 78 of ERS-1 and ERS-2 satellites of the European Space Agency. This track is centered on the Dead Sea and is aligned parallel to its axis (Figure 1). We processed 32 double-framed (200 km \times 100 km) images, acquired between 1992 and 2001, using the GAMMA processing software [*Wegmuller et al.*, 1998] and generated 163 geocoded unwrapped interferograms, with perpendicular baselines shorter than 300 m (Figure 3). We removed the first order orbital phase contributions using the Delft ERS precise orbital data [*Scharroo and Visser*, 1998], and corrected the topographic phase contribution using the Shuttle Radar Topographic Mission (SRTM) 3 arc-second Digital Elevation Model (DEM) (<http://www.cgiar-csi.org/data/elevation/item/45-srtm-90m-digital-elevation-database-v41>).

[7] Interferograms were processed in 2×10 (range by azimuth) looks, and filtered twice using an adaptive filter function based on the local fringe spectrum [*Goldstein and Werner*, 1998]. The dimensions of the first and subsequent

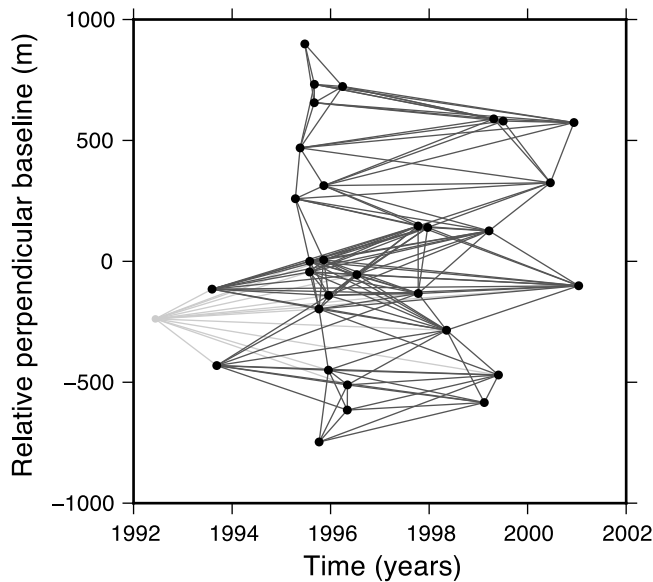


Figure 3. ERS-1 and ERS-2 images and interferograms for descending track 78. Relative perpendicular baselines and acquisition times are shown for all available double frame images. Images and interferograms used in this study are shown in black and dark gray, respectively, and the image and interferograms excluded from this study are shown in light gray.

filtering windows are 128×128 and 24×24 pixels, respectively. The resulting coherence map, taken as a proxy for filtering efficiency, is shown in Figure 4a, and is compared to coherence maps that result from single application of filtering using either a 36×36 or a 128×128 window (Figures 4b and 4c). Note that using this filtering approach, i.e., a large window followed by a smaller one, efficiently removes the high frequency noise, and consequently helps to expand the unwrapped area.

[8] Interferogram unwrapping was first carried out with the minimum cost flow and triangulation algorithms of *Werner et al.* [2002] on highly coherent areas (>0.5). Occasional unwrapping errors were corrected manually. Following geocoding of unwrapped interferograms to the DEM geometry, we re-sampled each interferogram onto 16×16 pixels windows (corresponding to a pixel size of $\sim 315 \times 315$ m²).

[9] In the proceeding, we impose a linearity constraint on the LOS velocity solution. This linearity constraint is only sensible to the extent that the water-level drop is constant. Indeed, inspection of the water-level record reveals that the water-level has dropped at a nearly constant rate between 1993 and 2001, but has increased during 1992 (Figure 2). For this reason we excluded an image acquired on 1992 and the 14 interferograms that include this image. Thus, of the 163 available interferograms composed of 32 images, we have used only 149 interferograms composed of 31 image acquisitions (Figure 3). A list of all the interferograms used in this study, along with their temporal and perpendicular baselines are detailed in Table S1 of the auxiliary material.¹

¹Auxiliary materials are available in the HTML. doi:10.1029/2011JB008961.

2.2. GPS

[10] We used 30-s continuous GPS data from the Geodetic Survey of Israel and analyzed in daily batches by SOPAC (<http://sopac.ucsd.edu>) as part of its Eastern Mediterranean regional network and in combination with other global and regional subnetworks using the GAMIT software [*Herring et al.*, 2010]. For this study, we performed a Principal Component Analysis (PCA) [*Dong et al.*, 2006] using as input the daily position time series from 18 stations in Israel processed by SOPAC and available from the GPS Explorer data portal (<http://geoapp03.ucsd.edu/gridsphere/gridsphere>). The oldest stations have data since 1997, while the newer stations began recording in 2006, so that each station has at least 5 years of continuous data. Using Jet Propulsion Laboratory's *st_filter* software, we solved for the first two principal components, while simultaneously estimating secular rates, annual and semi-annual terms, and offset parameters as needed to model GPS antenna changes and other non-tectonic effects. The PCA allowed us to identify and estimate offsets at several critical stations that had not been identified in the unfiltered SOPAC time series analysis. The complete set of filtered GPS time series and the time series analysis model terms can be found at GPS Explorer.

[11] We show in Figure 5 the filtered vertical component time series of station DRAG located on the Dead Sea's western coast (Figure 1), which shows an uplift rate of 2.75 ± 0.13 mm/yr with respect to TELA (Figure 5). The 1σ uncertainties are computed using a white noise plus flicker noise model to account for colored noise in the daily position time series [*Williams et al.*, 2004]. In the proceeding we will use this result to justify a linearity constraint on the LOS velocity, i.e., that the displacement rate resulting from the sea level drop is indeed constant.

3. Scheme to Extract LOS Change Rates

[12] Resolving the ground displacement due to Dead Sea water-level drop is hampered by several complications. First, the maximum displacement rate is expected to be just a few millimeters per year (see section 5.2). Second, the atmospheric noise is high due to low elevation and the presence of a large body of salt water with high evaporation rate. Third, the local topography is anti-correlated with the expected ground displacement (Figure 6), introducing a strong trade-off between the displacement and the topography-related atmospheric delay. To overcome these difficulties, we first correct each interferogram for a residual orbit phase, as described below. Next, we use time series analysis to calculate the phase change for each SAR acquisition. Finally, we simultaneously solve for the LOS velocity, DEM errors and the phase-elevation correlation, with the LOS velocity being subject to a linearity constraint supported by the CGPS analysis in the previous section. The LOS velocity and DEM errors are solved for each pixel independently, whereas the phase-elevation correlation is solved for each SAR acquisition independently. Using this approach we were able to separate the stratified atmospheric delay from the ground displacement.

3.1. Orbital Error Correction

[13] The accuracies of the satellite's orbits used in this study are 5–7 cm in the radial direction and 10–15 cm in the

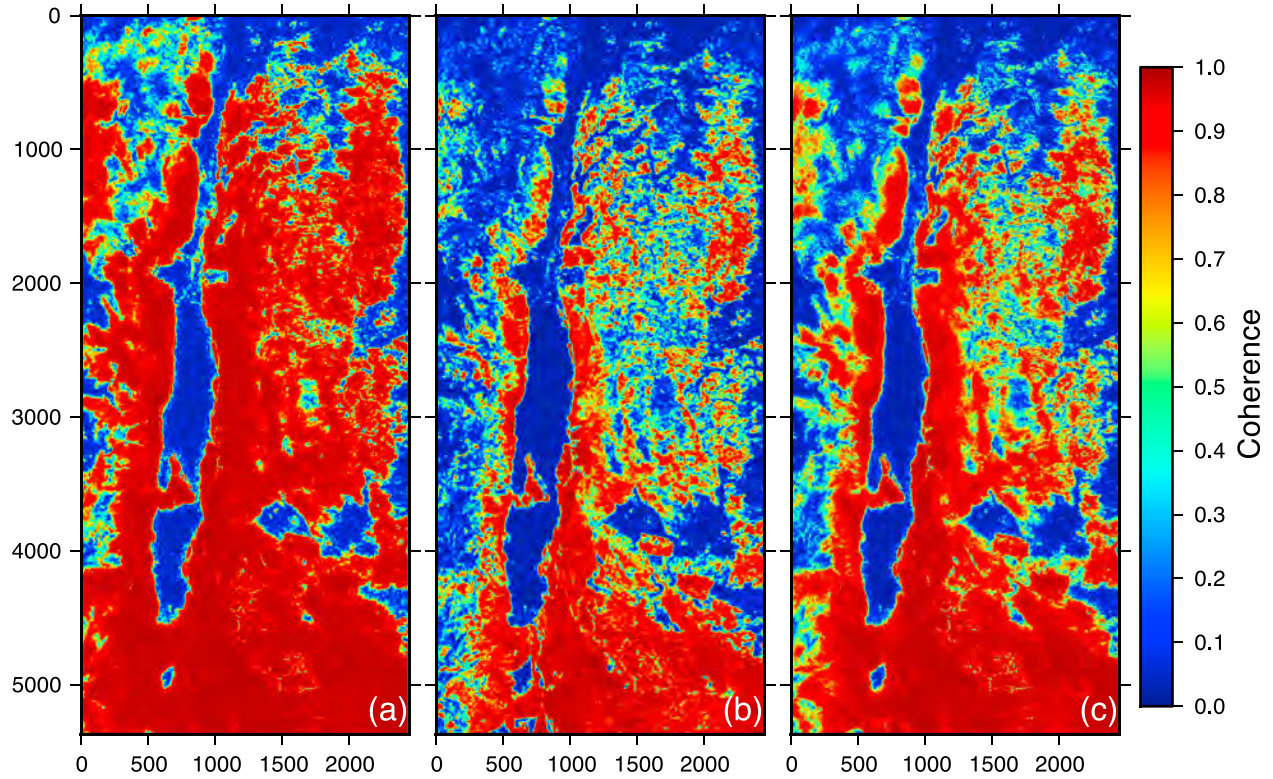


Figure 4. Coherence maps of interferogram 920611–950729 obtained using different filtering approaches. (a) Use of a 128×128 pixels filtering window followed by 24×24 window results in 73% of the pixels having coherence greater than 0.5. (b) Use of 36×36 pixels window (ROI-PAC's default window size) results in 45% of the pixels having coherence greater than 0.5. (c) Use of a 128×128 pixels filtering window results in 58% of the pixels having coherence greater than 0.5. Maps are in master image (920611) radar coordinates. Axes show pixel coordinates from top-left corner.

cross-track direction [Scharroo and Visser, 1998], resulting in errors in the perpendicular baseline and a long wavelength phase contribution to the interferogram [Hanssen, 2001; Biggs et al., 2007; Goumelen et al., 2010]. For the given accuracies, Hanssen [2001] predicts a contribution of about 1.5 fringe cycles (~ 42 mm) across a 100×100 km² frame. The removal of orbital errors in the interferometric phase is described below.

[14] Following Cavalié et al. [2008], we express the differential interferometric phase at pixel p of interferogram i , ϕ_{ip} , as a sum of four terms:

$$\phi_{ip} = [\alpha_i x_p + \beta_i y_p + \gamma_i (xy)_p + \delta_i] + \lambda_i z_p + \text{deformation}_{ip} + \text{noise}_{ip}, \quad (1)$$

where x , y and z are the coordinates along the east direction, the north direction and the elevation, respectively, and the symbols α , β , γ , δ , λ are the least squares fitting coefficients. The square-bracketed term describes a bi-linear ramp that accounts for the orbital errors as well as other long wavelength patterns, the second term accounts for the topography dependent atmospheric delay, and the remaining terms are self-explanatory (note that at this stage the DEM error is included within the noise term). The least squares adjustment is performed outside the interferogram central area (see

dashed rectangle in Figure 7a), i.e., where the deformation due to sea level drop is expected to be negligible. The orbital error corrected phase, ϕ_{ip}^* , is thus

$$\phi_{ip}^* = \phi_{ip} - [\alpha_i x_p + \beta_i y_p + \gamma_i (xy)_p + \delta_i]. \quad (2)$$

In Figure 7 we show an example interferogram, the bi-linear ramp, the orbit corrected interferogram resulting from application of the above procedure and the phase-topography correlation. Note the dramatic difference between the interferometric phase map before and after the application of the orbital error correction. Following the orbital error correction, the interferometric phase is referenced to the average phase outside the dashed rectangle in Figure 7a, but still includes contributions from topography dependent atmospheric delay and other noise.

3.2. Time Series Analysis

[15] For each pixel whose coherence exceeds 0.5 in all interferograms, we independently solve for the incremental phase change between successive acquisitions, $\Delta\phi$, via solution of [Schmidt and Bürgmann, 2003]

$$\phi_i^*(j, k) = G_i l(j, k) \Delta\phi_i, \quad (3)$$

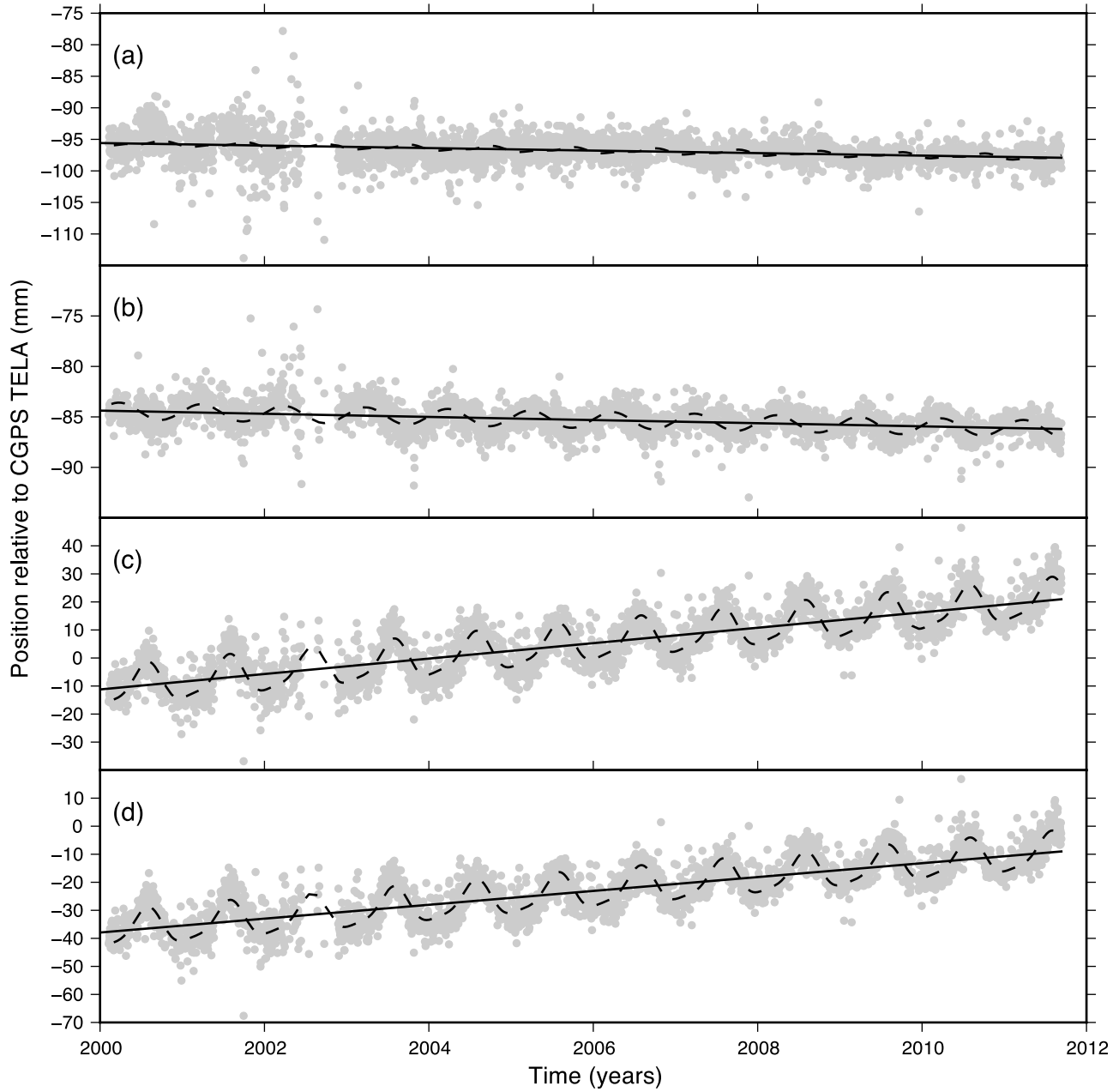


Figure 5. DRAG GPS site position relative to TELA (Figure 1). Time series (gray dots), with linear and sinusoidal best fits shown in dashed and solid lines, respectively. (a) East component, (b) north component, (c) up component, and (d) all components projected onto the satellite LOS.

where for interferogram i the j and k indexes correspond to the interferometric master and slave, respectively, and index l corresponds to the acquisition date. The matrix G is a design matrix whose size is equal to the number of interferograms times the number of acquisitions less 1, and its entries equal 1 for $j \leq l < k$, and 0 otherwise [López-Quiroz *et al.*, 2009]. The cumulative sum over the incremental phase change gives the time-dependent phase change with respect to the first acquisition in the set:

$$\Phi_{lp} = \sum_l \Delta\phi_{lp}. \quad (4)$$

In addition to the cumulative displacement with respect to the first date, these phase changes include contributions due to DEM errors that are proportional to the perpendicular baseline with respect to the first acquisition, atmospheric delays with respect to the first date and noise. Below we describe a new scheme for removing contributions to the phase due to DEM errors and atmospheric phase delays, whose key element is that the LOS change rate and the elevation-phase correlation slope are solved simultaneously (and not stepwise as is done by *Cavalié et al.* [2007] and *Elliott et al.* [2008]). While the former is solved for each pixel independently, the latter is solved for each SAR acquisition independently.

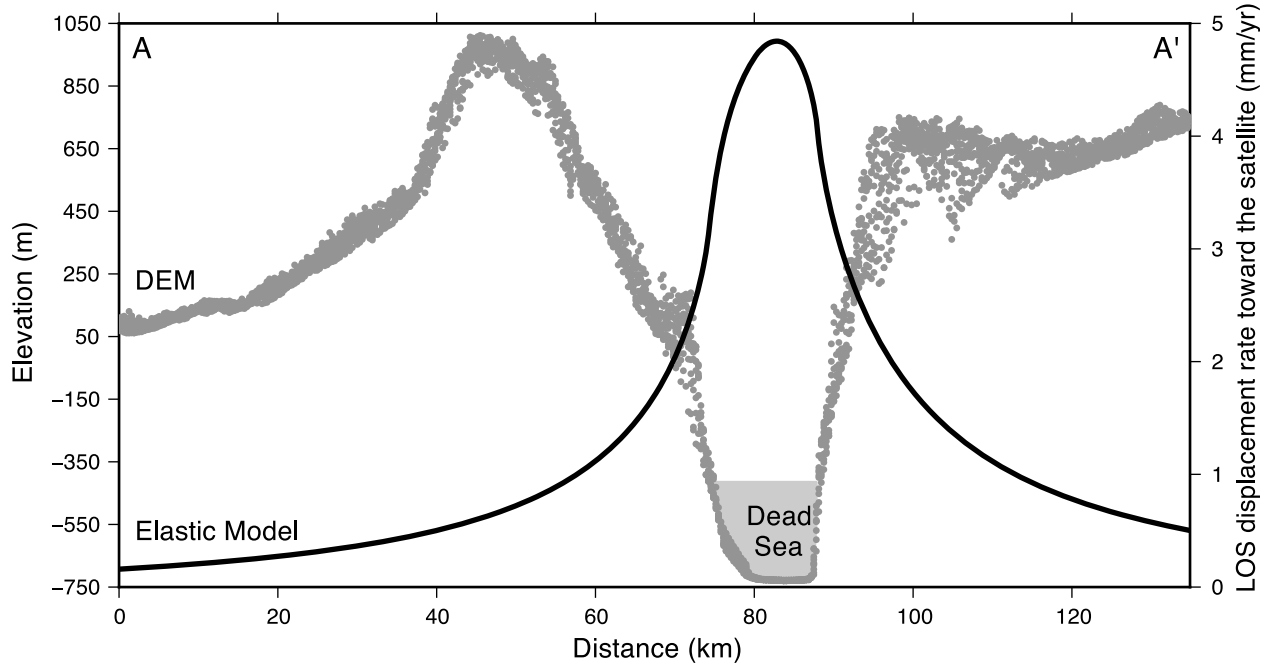


Figure 6. Profiles of predicted LOS change rate and elevation. The predicted LOS change rate is calculated for elastic homogenous half-space with Young modulus of 70 GPa and Poisson's ratio of 0.25 (solid line). The elevation (gray dots) is shown for pixels within a kilometer wide strip centered about A-A' profile, whose location is shown in Figure 1.

3.3. Resolving the Deformation Amid a Strong Trade-Off With Phase Delay Due to Stratified Atmosphere

[16] We impose a linearity constraint on the LOS change velocity. We think that this simplification is justified because the sea level has dropped at a nearly constant rate during the data interval examined in this study (Figure 2), and because the DRAG GPS station, located very close to the Dead-sea shoreline, is moving at a nearly constant rate (Figure 5). While the interval of DRAG data (2000–2011) has only a minor overlap with our InSAR images, the rate of sea level drop (about 1 m per year) was approximately similar in the two periods and thus constant since 1992 (Figure 2). Note, however, that a direct comparison between the GPS velocity in DRAG and the InSAR LOS velocity that will be presented below is not straightforward, since the two are not in the same reference frame.

[17] Two different effects contribute to the atmospheric phase delay; the first is turbulent mixing and the second is vertical stratification [Hanssen, 2001, and references therein]. While the former is complicated to remove directly and is often treated as a random noise that may be reduced by data stacking [e.g., Zebker et al., 1997; Fialko, 2006; Puysségur et al., 2007], the latter is proportional to the topography and may often be inferred from elevation versus phase diagrams [e.g., Delacourt et al., 1998; Remy et al., 2003; López-Quiroz et al., 2009].

[18] Because the topography in the Dead Sea area is almost a mirror image of the expected ground displacement (Figure 6), the use of elevation versus phase correlation to correct the topography-dependent atmospheric contribution,

may lead to the removal of the ground displacement along with the atmospheric delay. In addition, it is not justified to use a single elevation-phase correlation variable for the entire interferogram, since the climatic conditions are different between the east side of the Judea Mountains and the west side.

[19] To address this issue, we define a region of interest around the Dead Sea northern basin, where most of the ground displacement is expected to occur (dashed rectangle in Figure 8). Because that area is much smaller than the entire image and the climatic conditions within that area are more or less uniform for similar elevation areas, we expect the effect of topography-dependent stratified atmosphere to be uniform as well. Since performing the following calculation on the entire set would be computationally heavy, we select a subset of about 300 (almost) regularly spaced pixels within the region of interest (Figure 9) and solve simultaneously for the pixel's LOS change rates, V , the topography versus phase correlation of each acquisition with respect to the first image, S , the DEM error, D , and a constant C that corresponds to the noise of the first acquisition, using

$$\Phi_{lp} = (t_l - t_1)V_p + z_p S_l + b_l D_p + C_p, \quad (5)$$

where capital letters indicate the free parameters, t is the time of image acquisition, z is elevation, b is the perpendicular baseline with respect to the first acquisition, and l and p indexes correspond to the acquisition date and the pixel, respectively. The above equation is over-determined, and may be solved using a standard least squares algorithm. There is a risk that if the stratified atmospheric phase delay

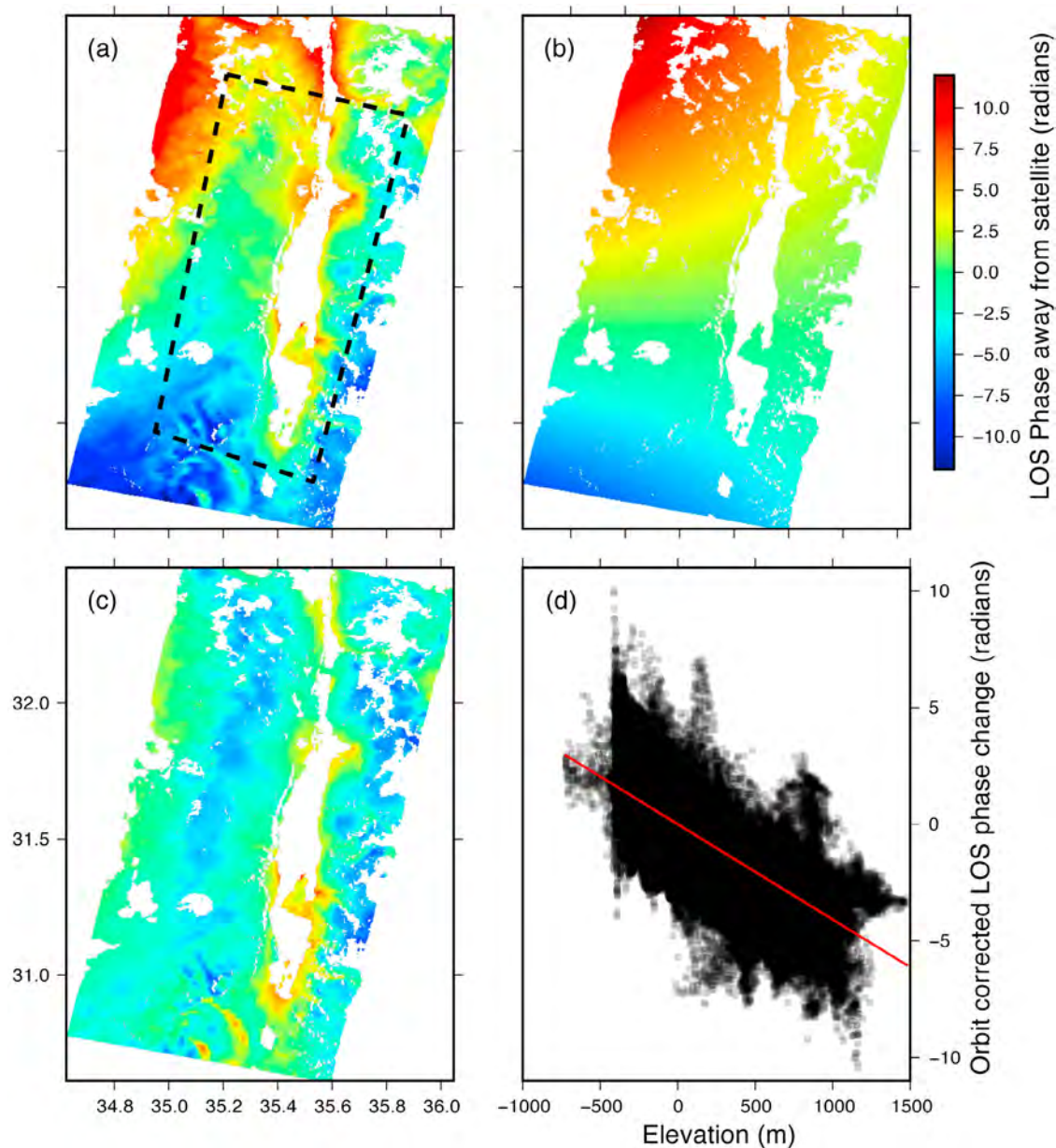


Figure 7. Example interferogram 951216–980510 and its applied corrections. (a) Unwrapped geocoded differential interferogram, with dashed rectangle indicating the area excluded from the calculation of the residual orbit correction (see section 3.1). (b) The bi-linear ramp accounting for residual orbit phase (bracketed term in equation (1)). (c) Unwrapped interferogram after corrections due to orbit uncertainties. (d) Phase versus elevation after the application of the residual orbital correction. The slope of the red straight line corresponds to the phase-elevation slope (λ) in equation (1).

factor, S , is time-dependent, the linear part of its time-dependency will “leak” to the deformation term in equation (5). Indeed, there is a possibility that the ongoing sea level drop causes a water surface area reduction that may give rise to an ongoing decrease in the evaporation rate and therefore also the atmospheric volatile content. A consequence of this process is that the atmospheric phase delay will decrease with time, and will be misinterpreted as LOS shortening, i.e., uplift. To see if there is such a significant long-term change in the volatile content we examined records of the relative humidity measured at a meteorological buoy that is located

within the Dead Sea northern basin. Inspection of these records reveals large fluctuations in the relative humidity, with a slight (statistically insignificant) long-term increase [Hect and Gertman, 2003]. In addition, we approximated the total evaporating water volume (using the mass balance equations in section 5.1) for intervals of 6 months, and did not find any significant linear trend (phase-elevation slope as a function of time is shown in Figure S1 in the auxiliary material). For these reasons it is safe to assume that the atmospheric phase contribution is not time-dependent.

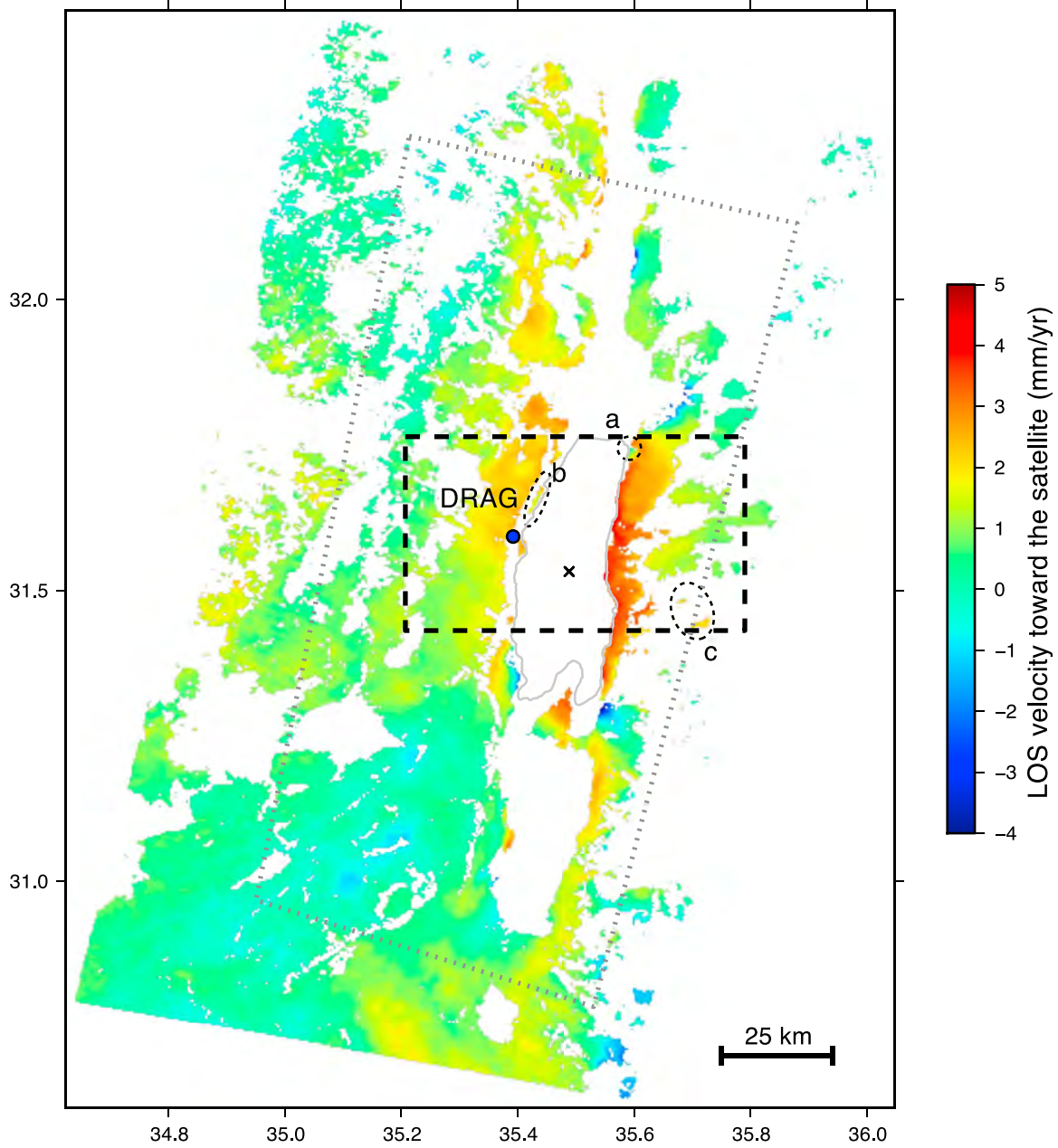


Figure 8. LOS velocity map (positive toward satellite). The dotted gray rectangle indicates the area excluded from the calculation of the residual orbit correction (see section 3.1). Dashed rectangle indicates the region of interest, where the velocity map is most reliable. Blue circle indicates the location of DRAG GPS site. X marks the center of removed mass. Areas a, b and c are small isolated patches that stand out with respect to their surroundings (see text and Figure 9). Gray contour marks the water-level at 415 m below MSL (corresponding to the year 2001).

[20] Next we subtract the phase-elevation term (second term on the right-hand side) to obtain the atmosphere corrected time-dependent phase:

$$\Phi_{lp}^* = \Phi_{lp} - z_p S_l. \quad (6)$$

Finally, we solve the following set for all pixels independently (both within and outside the region of interest):

$$\Phi_{lp}^* = (t_l - t_1) V_p + b_l D_p + C_p. \quad (7)$$

Using the above scheme we recover the part of the ground displacement whose rate is constant.

4. LOS Velocity Map

[21] The map of LOS change rate is shown in Figure 8. Recall that the phase correction due to stratified atmosphere is calculated solely for the area of interest (dashed rectangle of Figure 8). Thus the velocity map is mainly reliable within that area, and potentially interesting deformation patterns

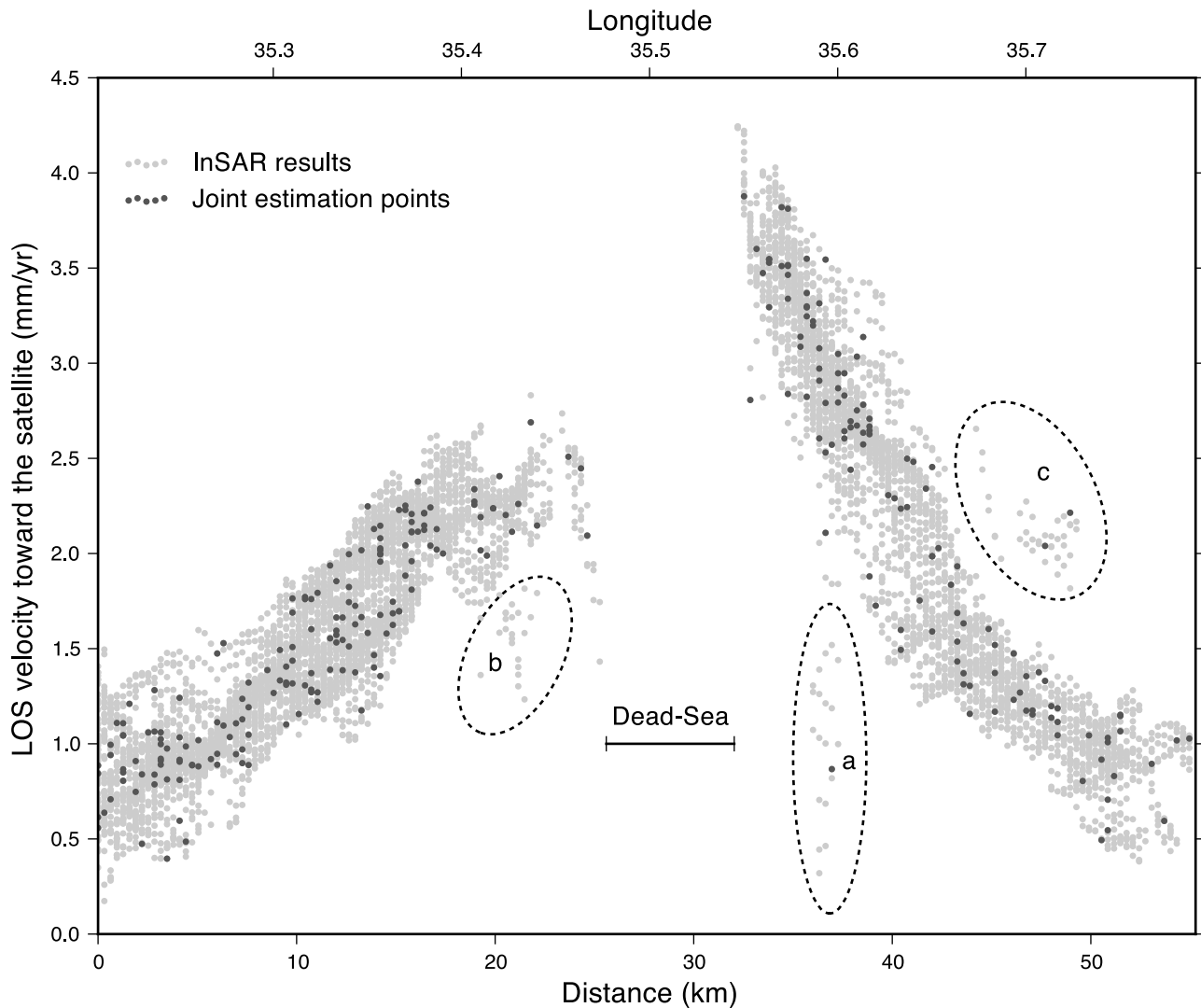


Figure 9. West-east profile of LOS change rate within the region of interest (see Figure 8 for location). Light gray dots show the velocity of all valid pixels. Dark gray dots indicate the sub-set of pixels used in equation (5) (see section 3.3 for more details). Dashed circles labeled a, b and c indicate the corresponding areas in Figure 8.

outside that area (some of which were identified in previous studies [e.g., Baer *et al.*, 2002; Abelson *et al.*, 2003]) are beyond the scope of this study.

[22] The maximum uplift rates at the Dead Sea northern basin are found near the shorelines (Figure 9). It is interesting to note that such a pattern has not been identified in any of the individual interferograms, including those with the longest time span. Several small isolated areas clearly stand out with respect to their surroundings (marked a, b and c in Figures 8 and 9). The subsidence in area a is due to local deformation near the Dead Sea shoreline, whose origin is yet to be determined, and the anomalous velocities in areas b and c are attributed to local unwrapping errors.

[23] We perform a bootstrapping test in order to rule out the possibility that the results are dominated, or strongly affected by a single image. The test proceeds according to the following steps: (a) Selection of one image at a time and removal of all the interferograms associated with that image from the set of interferograms (removing more than a single

image at a time results in a frequent occurrence of missing links between interferograms comprising the data set); (b) Recalculation of the LOS velocity as described in section 3; and (c) Calculation of an LOS velocity running average as a function of distance from the center of the removed water mass. In Figure 10 we compare the original profile (black curve) with that of the 31 profiles resulting from this test (gray curves). Note that the dominant pattern of uplift, that is strongest near the Dead Sea shoreline and decays with increasing distance, cannot be attributed to a single anomalous acquisition. Together, the result of the bootstrapping test and the fact that a pattern similar to the LOS change rate shown in Figure 8 map is not obvious in any of the individual interferograms indicate that the LOS change rate that we obtained is not an artifact of atmospheric noise.

[24] Finally, in order to see the benefits of the atmospheric correction in equations (5)–(6) and the DEM error correction in equation (7), we present in the auxiliary material the LOS velocity profile resulting from solution of equation (7)

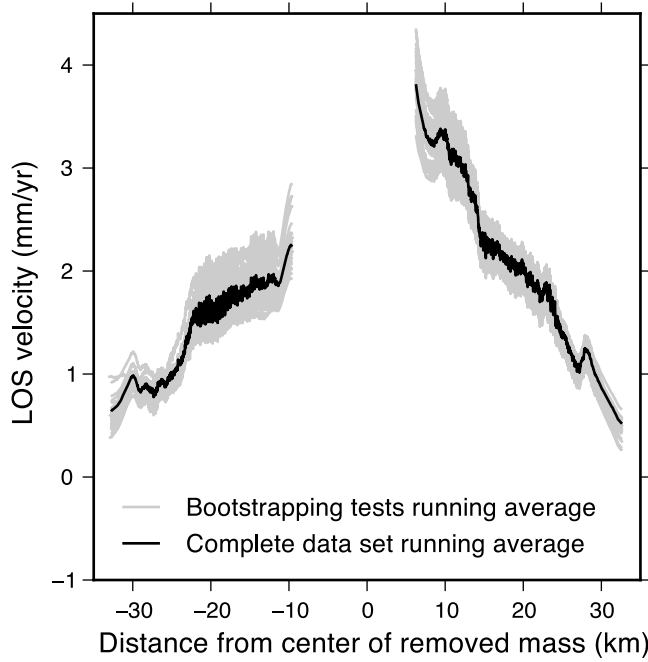


Figure 10. Result of bootstrapping tests. Running average profile of LOS change velocity as a function of distance from center of removed mass obtained using the entire data set (black curve) is compared to the running average profiles resulting from 31 bootstrapping tests (gray curves). Running averages are calculated for bins of 50 data points that are shifted by one data point each step. Note that the dominant pattern of uplift, that is strongest near the Dead Sea shoreline and decays with increasing distance, cannot be attributed to a single anomalous acquisition.

without performing the stratified atmosphere correction (Figure S2), and the LOS velocity profile resulting from solution of that equation after cancelling the DEM error term (Figure S3).

5. Geodynamic Implications

[25] The Dead Sea is a pull-apart basin that is undergoing subsidence and sedimentary filling since the Holocene, resulting in a negative mass anomaly that is much more significant than the water-level drop considered in this study. If this anomaly were to be compensated according to the Airy isostasy model, upper mantle should have reached to a depth of 15 km [ten Brink *et al.*, 2006]. Seismic studies, however, place the Moho at a much greater depth of about 30 km [Ginzburg *et al.*, 1979; ten Brink *et al.*, 2006]. Thus, isostatic compensation is not a viable mechanism for the Dead Sea basin. Instead, the upper crust may be supported by either lithospheric rigidity or an alternative mechanism [ten Brink *et al.*, 2006].

[26] Can the inferred crustal uplift due to the Dead Sea water-level drop be explained by a purely elastic model? To address this question we calculate the total vertical load change resulting from the combined effect of water removal and chemical precipitation within the Dead Sea northern basin. We then model the effect of applying the inferred load change on a homogeneous elastic half-space, and search for

a combination of elastic moduli that minimizes the difference between modeled and observed LOS changes.

5.1. Mass Balance and Loading

[27] Since the year 1979 the mass water balance within the Dead Sea northern basin is controlled mainly by water supply from the Jordan River and other smaller sources, natural evaporation and water consumption by the Israeli and Jordanian mineral industries. The mineral industries pump saline water from the northern basin into the evaporation pans in the southern basin and reject the end brine (of higher salinity) back to the northern basin. In addition during the last decades, halite precipitation has effectively raised the bottom of the lake by 0.1 m/year [Lensky *et al.*, 2005]. We calculate the total load change taking into account in situ evaporation, inflow and outflow of water of different densities, salt precipitation at the lake-bottom and progressive reduction in lake area.

[28] We use the Dead Sea water-level record (Figure 2) and the bathymetry map of Hall [1996] re-sampled to the DEM geometry. For each successive lake level record for 6 months intervals, adjusting the Dead Sea surface area each time. Finally, from this number we subtract 0.05 m to account for the halite precipitation that raises the sea bottom during that interval. Had evaporation and halite precipitation been the only processes accounting for the water-level change, the resulting load change at pixel p would be

$$\Delta\sigma_p^{\text{evaporation}} = \rho_{\text{water}} g \sum_n (h_{pn} - 0.5h_{\text{halite}}), \quad (8)$$

where ρ_{water} is the density of pure water, g is the gravitational acceleration, h_{halite} is the thickness of the halite layer added to the lake each year and h_{pn} is the time varying water-level change (positive if sea level rises), with the subscript n being the index of the 6 months interval.

[29] Fresh water evaporation, however, is not the only process accounting for the water-level change. Industrial pumping removes an annual volume of $500 \times 10^6 \text{ m}^3$ of saline water with density of 1240 Kg/m^3 . At the end of the industrial process, a volume of $250 \times 10^6 \text{ m}^3$ of end brine, with density of 1350 Kg/m^3 is rejected back to the Dead Sea [Lensky *et al.*, 2005]. The load change due to density and volume differences of pumped and rejected water masses is

$$\Delta\sigma_p^{\text{industrial}} = g \left[\sum_n \frac{0.5(V_{\text{reject}}\rho_{\text{reject}} - V_{\text{pump}}\rho_{\text{pump}})}{A_n} + \rho_{\text{water}} \sum_n \frac{0.5(V_{\text{pump}} - V_{\text{reject}})}{A_n} \right], \quad (9)$$

where A_n is the time varying lake area, V_{pump} and V_{reject} are the pumped and rejected volumes (per year), respectively, and ρ_{pump} and ρ_{reject} are the pumped and rejected densities, respectively. Finally, the total load change is a sum of the two processes:

$$\Delta\sigma = \Delta\sigma^{\text{evaporation}} + \Delta\sigma^{\text{industrial}}. \quad (10)$$

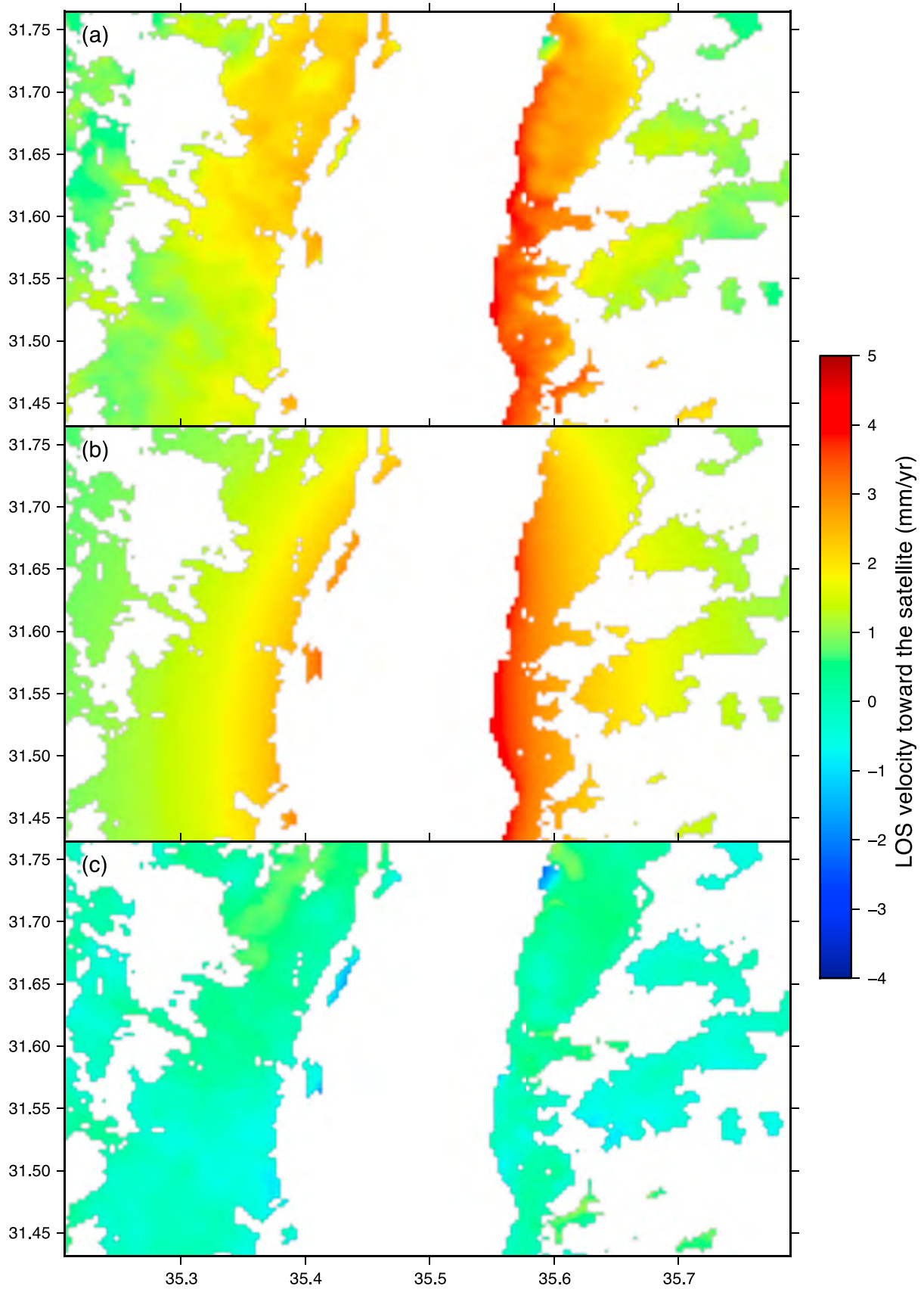


Figure 11. Comparison between observed and modeled LOS velocities. (a) Observed LOS velocity. (b) Best fit homogeneous elastic half-space model with Young modulus of 44 GPa and Poisson's ratio of 0.31. (c) Residual map at the region of interest (dashed rectangle in Figure 8).

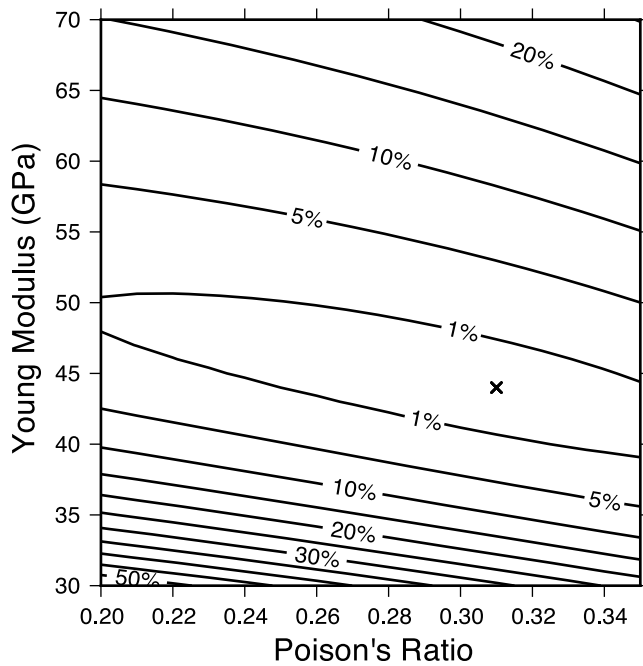


Figure 12. Contour plot of the percentage of misfit difference with respect to that of the best model as a function of the model's Young modulus and Poisson's ratio. X indicates the best fitting model.

Note that because the net effect of this process is to unload the ground surface, the sign of $\Delta\sigma$ is negative.

5.2. Homogeneous Elastic Model

[30] The 3-D displacement field resulting from the vertical unloading obtained in the previous section is computed atop of an elastic pre-stressed Cartesian box [Cavalié *et al.*, 2007]. The solved Navier equation includes the effect of

depth-dependent buoyancy contrasts, but neglects the effect of self-gravitation that is negligible for the wavelengths relevant here. The system is solved by 2-D Fourier transformation in the two horizontal directions. The kernels of sinusoidal surface loads are then computed by integrating a propagation matrix [Cathles, 1975] with a prescribed top normal stress, a zero top tangential stress, and a no-slip bottom boundary conditions. In order to avoid edge effects, we set the model dimensions to be much larger than the Dead Sea basin. The model vertical dimension is 300 km with 2 km grid spacing, and the model horizontal dimensions are $323 \times 323 \text{ km}^2$ with 315 m grid spacing (similar to the data spacing). The modeled ground displacements are calculated at surface grid points within an area that corresponds to the data frame, and are converted to LOS change. Since the observed velocities are relative to the frame edges, which do not extend to the edge of the deforming area, we add a constant to the observed velocity field that minimizes the Root Mean Square (RMS) of the observed and modeled residual map within the region of interest (Figure 11). The best fitting model is obtained using a Poisson's ratio of 0.31 and a Young modulus of 44 GPa. Inspection of the RMS contour diagram on a Young modulus versus Poisson's ratio space reveals a clear trade-off between the two elastic constants (Figure 12). While the Poisson's ratio cannot be resolved, it is clear that for any realistic Poisson's ratio (between 0.2 and 0.35), the Young modulus is 30–40 percent lower than that of an average upper crust [Dziewonski and Anderson, 1981].

[31] In Figure 13 we show the modeled up, east and LOS velocity EW profiles passing through the center of removed mass. Note that the model predicts up to 5.5 mm/year sea-floor rising near the center of the removed mass. In addition, the predicted LOS velocity of pixels, which are located on either side of the Dead Sea and whose distance from the center of the removed mass is equal, differ by up to 0.6 mm/year. This asymmetry is due to pixels to the east of the Dead

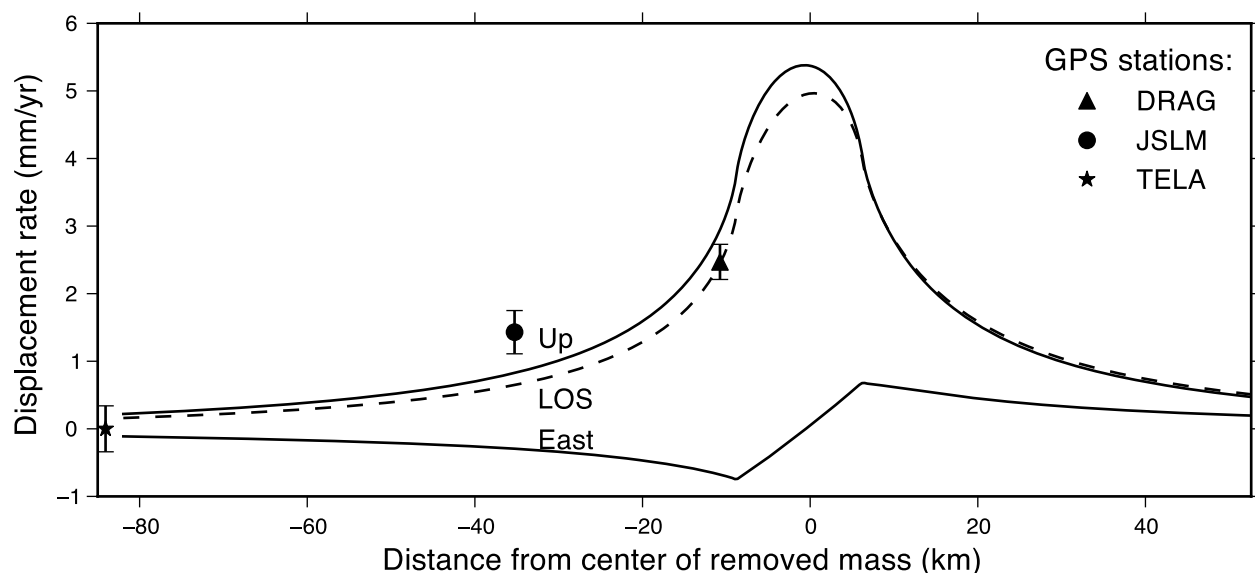


Figure 13. Modeled up component, east component and LOS displacement rate profiles, passing through the center of removed mass, using Young modulus of 44 GPa and Poisson's ratio of 0.31. Symbols indicate LOS projected velocities of GPS stations with respect to TELA and with a 2σ error bar.

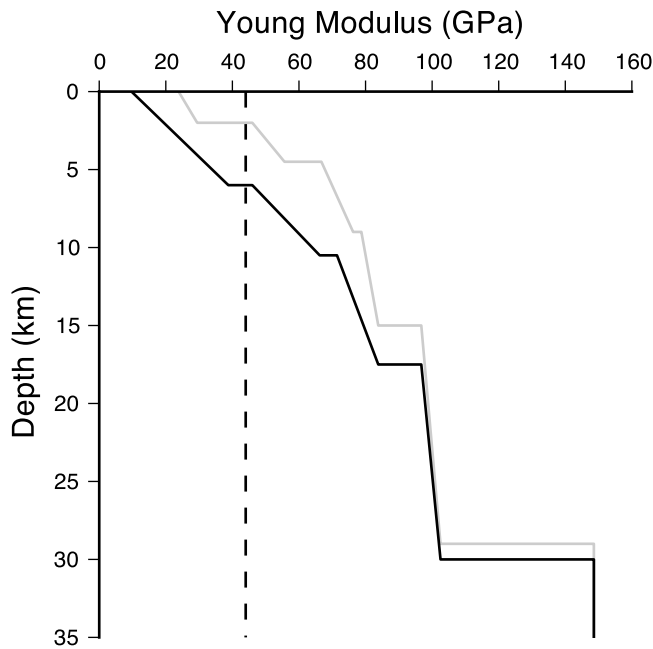


Figure 14. Depth-dependent Young modulus under the Dead Sea basin (solid dark curve, 3 in Figure 1a of *ten Brink et al.* [2006]) and under the western side of the Dead Sea (solid gray curve, 2 in Figure 1a of *ten Brink et al.* [2006]). Young moduli are inferred from seismic [*ten Brink et al.*, 2006] and gravity [*Götze et al.*, 2007] data. The dashed line indicates the Young modulus of the best fitting elastic model.

Sea moving by up to 0.75 mm/year toward the east, whereas pixels to the west moving by an equal amount to the west. Note that an asymmetric LOS change rate is also visible in the velocity map and profile (Figures 8 and 9) and the moving average profiles (Figure 10). This observed asymmetry is reproducible by the elastic model (Figure 11). However, because valid pixels closest to the center of removed mass are located on the eastern side, maximum LOS rate change east of the Dead Sea is by 2 mm/yr larger than that to its west. In addition, on Figure 13 we show the LOS velocities of three GPS stations forming a profile from the Dead Sea Western shore in station DRAG to the Mediterranean Sea in station TELA, passing through station JSLM in Judea Mountains (Figure 1). Note that the velocity of the latter exceeds the predicted velocity by about 0.9 mm per year. This discrepancy may be attributed to other deformation processes, such as the arching to the west of the Dead Sea transform that has been documented and modeled by [*Wdowinski and Zilberman*, 1996].

[32] It is somewhat surprising that a simple homogeneous elastic model provides a good fit to the data on both sides of the Dead Sea, since upper-crust seismic velocities inferred from seismic tomography indicate larger values east of the Dead Sea than west of it [*ten Brink et al.*, 2006], and since the Dead Sea transform juxtaposes Precambrian rocks in the east next to Paleozoic to Cenozoic sediments on the west [*Freund et al.*, 1970]. In Figure 14 we show profiles of Young modulus as a function of depth inferred from P wave velocities [*ten Brink et al.*, 2006] and densities [*Götze et al.*,

2007] using a Poisson's ratio of 0.31 (profiles locations are labeled as 2 and 3 on Figure 1a of *ten Brink et al.* [2006]). Note that the inferred Young modulus within the Dead Sea basin (solid dark curve in Figure 14) is by more than a factor of two lower than that of the best fitting model for depths lower than about 3 km, and that the depth-averaged Young modulus is similar to that of the best fit model down to about 15 km. Thus, that a simple homogeneous elastic model provides good fit to the data strongly suggests that the response of the crust to the sea level is controlled mainly by the elastic properties of the upper 15 km immediately below the Dead Sea basin.

[33] In order to assess the possibility that the above result is indeed most sensitive to the elastic properties of the top 15 km and is nearly insensitive to increasing the stiffness below that depth, we carried out a depth-sensitivity test as follows: (a) Calculate the ground displacement rate resulting from the application of the inferred load at the surface of an elastic layer of thickness H that overlies a stiffer homogeneous elastic half-space. The Poisson's ratio is everywhere set equal to that of the best fitting model (0.31) and the Young moduli of the top layer and the underlying half-space are set equal to that of the best fitting model (44 GPa) and twice that much, respectively; (b) Project the 3D ground displacement rate to the LOS; (c) Apply a constant shift to the resulting map of LOS change rate, for valid pixels within the region of interest, in a manner that minimizes the RMS of the difference between the newly obtained LOS velocities, V^{test} ,

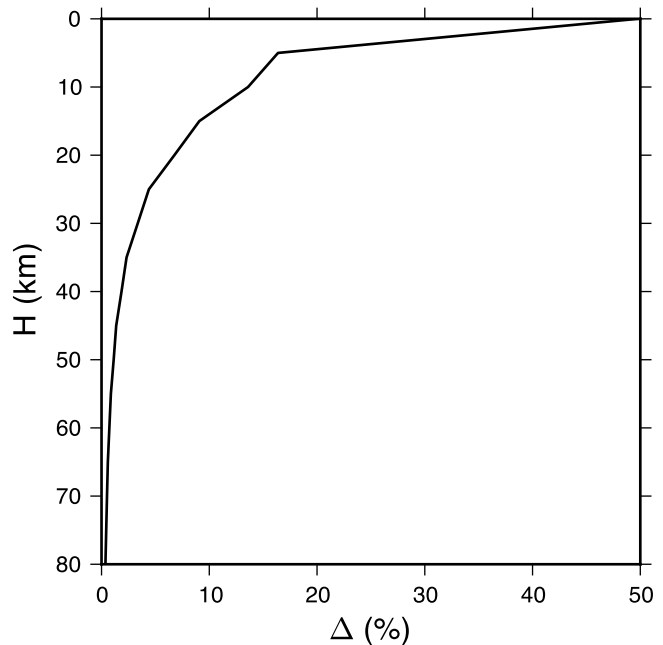


Figure 15. The results of the depth-sensitivity test. The percentage of the difference between the layered model velocities and the best fitting homogeneous model, Δ (see text), is shown as a function of the top layer thickness, H . Note that while the effect of doubling the Young modulus for all depths (i.e., $H = 0$) results in a 50% misfit increase with respect to the best fitting model, the effect of doubling the Young modulus for depths greater than 15 km results in less than 10% misfit increase.

and that of the best fitting model, V_p^{best} (Figure 11b), and record the percentage of RMS change as follows:

$$\Delta = 100 \sqrt{\sum_p (V_p^{best} - V_p^{test})^2} / \sqrt{\sum_p (V_p^{best})^2};$$

(d) Finally, repeat steps a through c for increasing H (i.e., top layer thickness). A plot of Δ versus H (Figure 15) indicates that while the effect of doubling the Young modulus for all depths (i.e., $H = 0$) results in a 50% misfit increase with respect to the best fitting model, the effect of doubling the Young modulus for depths greater than 15 km results in less than 10% misfit increase.

[34] Finally, it is worth noting that the crustal response to the Dead Sea water-level drop may also be reproducible by other models, incorporating time-dependent rheologies (e.g., visco-elasticity). However, because we impose a linearity constraint on the velocity analysis, and the retreat of the Dead Sea during our study interval (and therefore also the loading applied at the free surface) has occurred at a nearly constant rate, the result of this study is inadequate for constraining time-dependent rheologies.

6. Summary and Conclusions

[35] The Dead Sea water-level has been dropping at a constant rate of about 1 m per year since 1993. Based on simple elastic calculations and previous geodetic studies [Cavalié et al., 2007; Doin et al., 2010], it is expected that such a water-level drop will cause a geodetically resolvable uplift having a wavelength of tens of kilometers. In quest for that response, we analyzed ground displacements in the Dead Sea area using 149 SAR interferograms, composed of 31 ERS-1 and ERS-2 images acquired between 1993 and 2001 and continuous GPS data from the Survey of Israel acquired from 1997 to 2011.

[36] The expected ground displacement was found to be as low as a few millimeters per year, and the data was extremely noisy due to atmospheric effects. In addition, with a topography that is a mirror image of the expected ground displacement, a strong trade-off was introduced between the topography and the phase contribution due to stratified atmosphere. Nonetheless, using a new analysis scheme, specifically tailored to address these difficulties, we have successfully estimated the ground displacements. A key element in our scheme is that we solve simultaneously for a constant LOS change rate (supported by the GPS results) and an elevation-phase correlation slope. The former is solved for each pixel independently, whereas the latter is solved for each SAR acquisition independently. With this approach we were able to remove the topography related atmospheric delay, while resolving the ground displacements.

[37] Inspection of our LOS change rate map clearly reveals uplift around the Dead Sea northern basin, with maximum LOS change rates near the eastern shoreline reaching about 4.3 mm/year and decaying gradually with increasing distance from the Dead Sea. We have performed a bootstrapping test in order to assess the possibility that the result is dominated by a single image, and concluded that our result is robust and cannot be attributed to a single acquisition date.

[38] Finally, we show that the crustal response to the Dead Sea water-level drop can be simulated by a homogeneous elastic half-space model, with a Young modulus of about 44 GPa. Such a modulus is compatible with that of the average Young modulus inferred from seismic and gravity data down to a depth of 15 km below the Dead Sea basin, suggesting that the response of the crust to the sea level is controlled mainly by the elastic properties of the upper 15 km immediately below the Dead Sea basin.

[39] **Acknowledgments.** This work is part of ESA project C1P.5544. We thank the Survey of Israel for continuous GPS data used in this study and to SOPAC staff (Linette Sternlicht and Melinda Squibb) for assistance in the GPS time series analysis. Y.B.'s participation is funded by NASA Measures grant NMO710973, JPL subcontract 1368580.

References

- Abelson, M., G. Baer, V. Shtivelman, D. Wachs, E. Raz, O. Crouvi, I. Kurzon, and Y. Yechieli (2003), Collapse-sinkholes and radar interferometry reveal neotectonics concealed within the Dead Sea basin, *Geophys. Res. Lett.*, **30**(10), 1545, doi:10.1029/2003GL017103.
- Baer, G., U. Schattner, D. Wachs, D. Sandwell, S. Wdowski, and S. Frydman (2002), The lowest place on Earth is subsiding—An InSAR (interferometric synthetic aperture radar) perspective, *Geol. Soc. Am. Bull.*, **114**(1), 12–23, doi:10.1130/0016-7606(2002)114<0012:TLPOEI>2.0.CO;2.
- Biggs, J., T. Wright, Z. Lu, and B. Parsons (2007), Multi-interferogram method for measuring interseismic deformation: Denali Fault, Alaska, *Geophys. J. Int.*, **170**(3), 1165–1179, doi:10.1111/j.1365-246X.2007.03415.x.
- Bills, B. G., and G. M. May (1987), Lake Bonneville: Constraints on lithospheric thickness and upper mantle viscosity from isostatic warping of Bonneville, Provo, and Gilbert stage shorelines, *J. Geophys. Res.*, **92**, 11,493–11,508, doi:10.1029/JB092iB11p11493.
- Cathles, L. M. (1975), *The Viscosity of the Earth's Mantle*, 386 pp., Princeton Univ. Press, Princeton, N. J.
- Cavalié, O., M.-P. Doin, C. Lasserre, and P. Briole (2007), Ground motion measurement in the Lake Mead area, Nevada, by differential synthetic aperture radar interferometry time series analysis: Probing the lithosphere rheological structure, *J. Geophys. Res.*, **112**, B03403, doi:10.1029/2006JB004344.
- Cavalié, O., C. Lasserre, M.-P. Doin, G. Peltzer, J. Sun, X. Xu, and Z. K. Shen (2008), Measurement of interseismic strain across the Haiyuan fault (Gansu, China), by InSAR, *Earth Planet. Sci. Lett.*, **275**(3–4), 246–257, doi:10.1016/j.epsl.2008.07.057.
- Delacourt, C., P. Briole, and J. A. Achache (1998), Tropospheric corrections of SAR interferograms with strong topography: Application to Etna, *Geophys. Res. Lett.*, **25**(15), 2849–2852, doi:10.1029/98GL02112.
- Doin, M.-P., C. Twardzik, G. Ducret, C. Lasserre, S. Guillaso, and S. Jianbao (2010), Visco-elastic rebound of the lithosphere around the lake Siling Co in Tibet observed by InSAR, Abstract G41B-0817 presented at 2010 Fall Meeting, AGU, San Francisco, Calif., 13–17 Dec.
- Dong, D., P. Fang, Y. Bock, F. Webb, L. Prawirodirdjo, S. Kedar, and P. Jamason (2006), Spatiotemporal filtering using principal component analysis and Karhunen-Loeve expansion approaches for regional GPS network analysis, *J. Geophys. Res.*, **111**, B03405, doi:10.1029/2005JB003806.
- Dziewonski, A. M., and D. L. Anderson (1981), Preliminary reference Earth model, *Phys. Earth Planet. Inter.*, **25**(4), 297–356, doi:10.1016/0031-9201(81)90046-7.
- Elliott, J. R., J. Biggs, B. Parsons, and T. J. Wright (2008), InSAR slip rate determination on the Altyn Tagh Fault, northern Tibet, in the presence of topographically correlated atmospheric delays, *Geophys. Res. Lett.*, **35**, L12309, doi:10.1029/2008GL033659.
- Fialko, Y. (2006), Interseismic strain accumulation and the earthquake potential on the southern San Andreas fault system, *Nature*, **441**(7096), 968–971, doi:10.1038/nature04797.
- Freund, R., Z. Garfunkel, I. Zak, M. Goldberg, T. Weissbrod, B. Derin, F. Bender, F. E. Wellings, and R. W. Girdler (1970), The shear along the Dead Sea Rift [and discussion], *Philos. Trans. R. Soc. A*, **267**(1181), 107–130.
- Garfunkel, Z. (1997), The history and formation of the dead sea basin, in *The Dead Sea: The Lake and Its Setting*, edited by T. M. Niemi, Z. Ben Avraham, and J. Gat, pp. 36–56, Oxford Univ. Press, Oxford, U. K.
- Ginzburg, A., J. Makris, K. Fuchs, C. Prodehl, W. Kaminski, and U. Amitai (1979), A seismic study of the crust and upper mantle of the Jordan-Dead

- Sea rift and their transition toward the Mediterranean Sea, *J. Geophys. Res.*, **84**, 1569–1582, doi:10.1029/JB084iB04p01569.
- Goldstein, R. M., and C. L. Werner (1998), Radar interferogram filtering for geophysical applications, *Geophys. Res. Lett.*, **25**(21), 4035–4038, doi:10.1029/1998GL900033.
- Götze, H.-J., R. El-Kelani, S. Schmidt, M. Rybakov, M. Hassounieh, H. J. Förster, and J. Ebbing (2007), Integrated 3D density modelling and segmentation of the Dead Sea Transform, *Int. J. Earth Sci.*, **96**(2), 289–302, doi:10.1007/s00531-006-0095-5.
- Gourmelen, N., F. Amelung, and R. Lanari (2010), Interferometric synthetic aperture radar–GPS integration: Interseismic strain accumulation across the Hunter Mountain fault in the eastern California shear zone, *J. Geophys. Res.*, **115**, B09408, doi:10.1029/2009JB007064.
- Hall, J. K. (1996), Digital topography and bathymetry of the area of the Dead Sea depression, *Tectonophysics*, **266**(1–4), 177–185, doi:10.1016/S0040-1951(96)00189-8.
- Hanssen, R. F. (2001), *Radar Interferometry: Data Interpretation and Error Analysis*, vol. 2, 328 pp., Kluwer Acad., Dordrecht, Netherlands.
- Hect, A., and I. Gertman (2003), Dead Sea meteorological climate, in *Fungal Life in the Dead Sea*, edited by E. Nevo, A. Oren, and S. P. Wasser, pp. 68–114, A.R.G. Gantner, Ruggell, Liechtenstein.
- Herring, T. A., R. W. King, and S. C. McClusky (2010), Documentation for the GAMIT GPS analysis software, Version 10.4, report, Mass. Inst. of Technol., Cambridge.
- Lambeck, K. (1991), Glacial rebound and sea-level change in the British Isles, *Terra Nova*, **3**(4), 379–389, doi:10.1111/j.1365-3121.1991.tb00166.x.
- Lambeck, K., C. Smither, and P. Johnston (1998), Sea-level change, glacial rebound and mantle viscosity for northern Europe, *Geophys. J. Int.*, **134**, 102–144, doi:10.1046/j.1365-246x.1998.00541.x.
- Le Beon, M., Y. Klinger, A. Q. Amrat, A. Agnon, L. Dorbath, G. Baer, J. Ruegg, O. Charade, and O. Mayyas (2008), Slip rate and locking depth from GPS profiles across the southern Dead Sea Transform, *J. Geophys. Res.*, **113**, B11403, doi:10.1029/2007JB005280.
- Lensky, N. G., Y. Dvorkin, V. Lyakhovsky, I. Gertman, and I. Gavrieli (2005), Water, salt, and energy balances of the Dead Sea, *Water Resour. Res.*, **41**, W12418, doi:10.1029/2005WR004084.
- López-Quiroz, P., M.-P. Doin, F. Tupin, P. Briole, and J. Nicolas (2009), Time series analysis of Mexico City subsidence constrained by radar interferometry, *J. Appl. Geophys.*, **69**(1), 1–15, doi:10.1016/j.jappgeo.2009.02.006.
- Mitrovica, J. X., and W. R. Peltier (1993), The inference of mantle viscosity from an inversion of the Fennoscandian relaxation spectrum, *Geophys. J. Int.*, **114**(1), 45–62, doi:10.1111/j.1365-246X.1993.tb01465.x.
- Nakiboglu, S. M., and K. Lambeck (1982), A study of the Earth's response to surface loading with application to Lake Bonneville, *Geophys. J.*, **70**(3), 577–620, doi:10.1111/j.1365-246X.1982.tb05975.x.
- Pe'eri, S., H. A. Zebker, Z. Ben-Avraham, A. Frumkin, and J. K. Hall (2004), Spatially resolved uplift rate of the Mount Sedom (Dead Sea) salt diapir from InSAR observations, *Isr. J. Earth Sci.*, **53**(2), 99–106, doi:10.1560/7B8G-6VFK-1GNH-QGF8.
- Peltier, W. R., R. A. Drummond, and A. M. Tushingham (1986), Post-glacial rebound and transient lower mantle rheology, *Geophys. J. R. Astron. Soc.*, **87**(1), 79–116, doi:10.1111/j.1365-246X.1986.tb04548.x.
- Puysségur, B., R. Michel, and J.-P. Avouac (2007), Tropospheric phase delay in interferometric synthetic aperture radar estimated from meteorological model and multispectral imagery, *J. Geophys. Res.*, **112**, B05419, doi:10.1029/2006JB004352.
- Remy, D., S. Bonvalot, P. Briole, and M. Murakami (2003), Accurate measurements of tropospheric effects in volcanic areas from SAR interferometry data: Application to Sakurajima volcano (Japan), *Earth Planet. Sci. Lett.*, **213**(3–4), 299–310, doi:10.1016/S0012-821X(03)00331-5.
- Sadeh, M. (2011), Crustal deformation along the Dead Sea Transform and Carmel Fault inferred from GPS measurements and elastic models, MSc thesis, 71 pp., Dep. of Geol. and Environ. Sci., Ben-Gurion Univ. of the Negev, Beer-Sheva, Israel.
- Scharroo, R., and P. Visser (1998), Precise orbit determination and gravity field improvement for the ERS satellites, *J. Geophys. Res.*, **103**, 8113–8127, doi:10.1029/97JC03179.
- Schmidt, D. A., and R. Bürgmann (2003), Time-dependent land uplift and subsidence in the Santa Clara valley, California, from a large interferometric synthetic aperture radar data set, *J. Geophys. Res.*, **108**(B9), 2416, doi:10.1029/2002JB002267.
- Sjöberg, L. E., M. Pan, E. Asenjo, and S. Erlingsson (2000), Glacial rebound near Vatnajökull, Iceland, studied by GPS campaigns in 1992 and 1996, *J. Geodyn.*, **29**(1–2), 63–70, doi:10.1016/S0264-3707(99)00061-7.
- ten Brink, U. S., A. Al-Zoubi, C. H. Flores, Y. Rotstein, I. Qabbani, S. H. Harder, and G. R. Keller (2006), Seismic imaging of deep low-velocity zone beneath the Dead Sea basin and transform fault: Implications for strain localization and crustal rigidity, *Geophys. Res. Lett.*, **33**, L24314, doi:10.1029/2006GL027890.
- Wachs, D., Y. Yechieli, V. Shtivelman, A. Itamar, G. Baer, M. Goldman, E. Raz, M. Rybekov, and U. Schattner (2000), Formation of sinkholes along the Dead Sea shore, Summary of findings from the first stage of research, *Rep. 41/2000*, 49 pp., Geol. Surv. of Israel, Jerusalem.
- Wdowinski, S., and E. Zilberman (1996), Kinematic modelling of large-scale structural asymmetry across the Dead Sea Rift, *Tectonophysics*, **266**(1–4), 187–201, doi:10.1016/S0040-1951(96)00238-7.
- Wdowinski, S., Y. Bock, G. Baer, L. Prawirodirdjo, N. Bechor, S. Naaman, R. Knafo, Y. Forrai, and Y. Melzer (2004), GPS measurements of current crustal movements along the Dead Sea Fault, *J. Geophys. Res.*, **109**, B05403, doi:10.1029/2003JB002640.
- Wegmüller, U., C. Werner, and T. Strozzi (1998), SAR interferometric and differential interferometric processing chain, in *Geoscience and Remote Sensing Symposium Proceedings, 1998. IGARSS '98. 1998 IEEE International*, pp. 1106–1108, Inst. of Electr. and Electr. Eng., New York.
- Weinberger, R., V. Lyakhovsky, G. Baer, and Z. B. Begin (2006), Mechanical modeling and InSAR measurements of Mount Sedom uplift, Dead Sea basin: Implications for effective viscosity of rock salt, *Geochem. Geophys. Geosyst.*, **7**, Q05014, doi:10.1029/2005GC001185.
- Werner, C., U. Wegmüller, T. Strozzi, and A. Wiesmann (2002), Processing strategies for phase unwrapping for INSAR applications, paper presented at European Conference on Synthetic Aperture Radar, Assoc. for Electr., Electr. and Inf. Technol., Cologne, Germany, 4–6 June.
- Williams, S. D. P., Y. Bock, P. Fang, P. Jamason, R. M. Nikolaidis, L. Prawirodirdjo, M. Miller, and D. J. Johnson (2004), Error analysis of continuous GPS position time series, *J. Geophys. Res.*, **109**, B03412, doi:10.1029/2003JB002741.
- Zebker, H. A., P. A. Rosen, and S. Hensley (1997), Atmospheric effects in interferometric synthetic aperture radar surface deformation and topographic maps, *J. Geophys. Res.*, **102**, 7547–7563, doi:10.1029/96JB03804.